Contents lists available at ScienceDirect

Cement and Concrete Research

In situ TEM observation of calcium silicate hydrate nanostructure at high temperatures

Qi Zheng [a,b], Jinyang Jiang [a,*], Xinle Li [c,1], Karen C. Bustillo [d], Haimei Zheng [b,*]

[a] *School of Materials Science and Engineering, Southeast University, Nanjing 211189, PR China*
[b] *Materials Sciences Division, Lawrence Berkeley National Laboratory, Berkeley, CA 94720, United States*
[c] *The Molecular Foundry, Lawrence Berkeley National Laboratory, Berkeley, CA 94720, United States*
[d] *National Center for Electron Microscopy, Molecular Foundry, Lawrence Berkeley National Laboratory, Berkeley, CA, USA*

A R T I C L E   I N F O

A B S T R A C T

Fire poses a substantial threat to concrete structures because calcium silicate hydrate (C-S-H) is not thermally stable at high temperatures. Herein, *in situ* TEM at temperatures from 20 to 800 °C was conducted to study the thermal-induced structural changes in C-S-H. We captured C-S-H shrinks at an average rate of 0.02 μm^2/°C upon heating with three stages observed, including induction, constant, and rapid periods. Our observation revealed that an 800 nm pore could be healed during pore structure evolution owing to the reconstruction and deformation among C-S-H blocks. The Ca/Si ratio was dropped at higher temperatures because of the leakage of calcium ions from the C-S-H structure to form CaO precipitates. The temperature-driven phase transformation and degradation were also detected using electron diffraction that C-S-H was transformed into metastable calcium silicate minerals above 800 °C. This work provides insights into the nanoscale transformation of C-S-H at high temperatures.

1. Introduction

The mechanical properties of concrete are often significantly compromised when the concrete is exposed to high temperatures. Concrete undergoes continuous irreversible decomposition reactions, resulting in an increase in porosity followed by the degradation of mechanical properties [1–4]. C-S-H is the main hydration product and the primary binding component in concrete [5], and it dictates the performance of concrete at the nanoscale [6]. Understanding the thermal stability of calcium silicate hydrate (C-S-H) is crucial for predicting concrete degradation at high temperatures. So far, the underlying mechanisms of the changes in chemistry, nanostructure, and morphology of C-S-H induced by thermal heating still needs to be enriched, especially at the nanoscale.

Thermogravimetric analysis (TGA) [7–9] has been recognized as a powerful tool to resolve the physical and chemical transformations at various temperatures. A typical TGA curve can be classified into several stages to evaluate the dehydration reactions of C-S-H [10,11]. These thermal analysis methods provide opportunities to investigate the effect of temperature on the composition of hydration products and determine the decomposition reactions of concrete under high temperatures. However, the weight loss recorded in the TGA curve is an average descriptor. Some essential information, such as the evolution of phase, morphology, elemental composition, and porosity, cannot be determined from the TGA measurements.

In situ experiments facilitate the assessment of C-S-H in a more native environment over time and thus allow for the study of complex phenomena involving phase and structure changes. For example, the composition and phase diagram in cement pastes up to 620 °C have been monitored by neutron diffraction [12]. *In situ* X-ray diffraction (XRD) was employed to investigate the transformation of C-S-H to wollastonite [13]. Recently, the thermoelastic properties of the portlandite from −100 to 700 °C were measured by Brillouin spectroscopy [14]. 3D analysis of moisture distribution in concrete was also achieved at high temperatures using *in-situ* neutron tomography [15]. These *in situ* studies have allowed tracking the structural transformation of concrete at various stages.

In this work, we investigate the heat-driven degradation of C-S-H in the temperature range of 20 to 800 °C using *in situ* TEM. The C-S-H sample at evaluated temperatures was imaged in real-time, allowing

---

tracing the morphology and pore structure evolution, element, and phase transformations. We did a quantitative analysis on kinetic properties like the shrinkage rate and reaction speed based on the evolutionary dynamics. This study offers an in-depth understanding of the nanoscale mechanisms of C-S-H at high temperatures, and it provides information such as structure, element, phase to rationalize the design of high-performance concrete serving in extreme conditions.

2. Materials and characterizations

2.1. Dilute hydration for producing C-S-H

Tricalcium silicate (C_3S) was prepared by Li's method [16]. C-S-H was synthesized by dilute hydration of C_3S at a solid to water ratio of 1:100. The suspension was sealed for a uniform reaction. After hydration for 30 days, the precipitates were collected and dried in a nitrogen environment for 48 h and kept in the glove box for further measurements. A solid powder sample was used for TGA, XRD, and FTIR measurements, and the sample was dispersed in isopropanol before being drop-casted onto a lacey carbon supported copper grid for TEM characterization.

2.2. Thermogravimetric analysis

TGA was performed on TA Instruments Q5500 TGA-MS (U.S.). The instrument is sensitive to <0.1 μg with a testing temperature up to 1200 °C. C-S-H measurement was conducted in a nitrogen atmosphere with a temperature range from ambient to 800 °C and a temperature ramp rate of 10 °C/min. The nitrogen flow rate was kept 25 ml/min in the measurement.

2.3. Powder X-ray diffraction

The Rigaku (Japan) Miniflex 6G XRD, a benchtop X-ray diffraction system, was used for C-S-H identification. It used a Cu K alpha radiation ($\lambda = 1.5418$ Å) with a 600 W X-ray source at 40 kV voltage and 15 mA current. The XRD pattern was collected in 1D mode over the range of $2\theta = 2\text{-}80^o$ (0.02^o per step), with a scanning speed of 2°/min. The powdered C-S-H sample was prepared by hand grinding to a fineness <50 μm and then pressed into a pellet in a specimen holder.

2.4. Fourier-transform infrared spectroscopy

The Nicolet iS50 FTIR from Thermo Fisher Scientific (U.S.) was employed to collect the infrared spectrum from 400 to 4000 cm^{-1} in transmission mode. All background and sample acquisitions were acquired at 8 cm^{-1} resolution with a minimum of 64 scans.

2.5. Transmission electron microscopy (TEM)

The Thermo Fisher Scientific (U.S.) ThemIS transmission electron microscope was used in our heating experiments. The microscope was operated at 300 keV with the image aberration corrector fully corrected for coherent axial aberrations up to 3rd order. The Bruker EDS detector, with a solid angle of 0.7 sr, enabled high count rates with minimal dead time for fast STEM-EDS mapping. Here, the dwell time was set 20 μs with drift correction enabled. For bright field imaging, the electron dose rate was ~11 e·Å^{-2}·s^{-1}. For electron diffraction, a 50 μm C2 aperture was used to limit the illuminated area.

2.6. In situ heating experiment

The Gatan 652 heating holder has a tantalum furnace designed to observe the microstructural phase changes at temperatures up to 1000 °C (Fig. 1A). The specimen was securely held in place using a threaded clamping mechanism to ensure good thermal contact between the specimen and the furnace. The low mass of the specimen furnace ensures a rapid response to changes in the heater current with a nonlinear relation, as shown in Fig. 1B. The rate of increase of specimen temperature was manually controlled, ranging from 0.5 to 1.0 °C/s. The sample was baked at the selected temperature for 15 min for stabilization. Finally, the TEM column was opened for *in situ* characterization (Fig. 1C) at the following ten temperatures: 20, 50, 100, 200, 300, 400, 500, 600, 700, 800 °C. The final anneal was performed at 400 °C for 9 h.

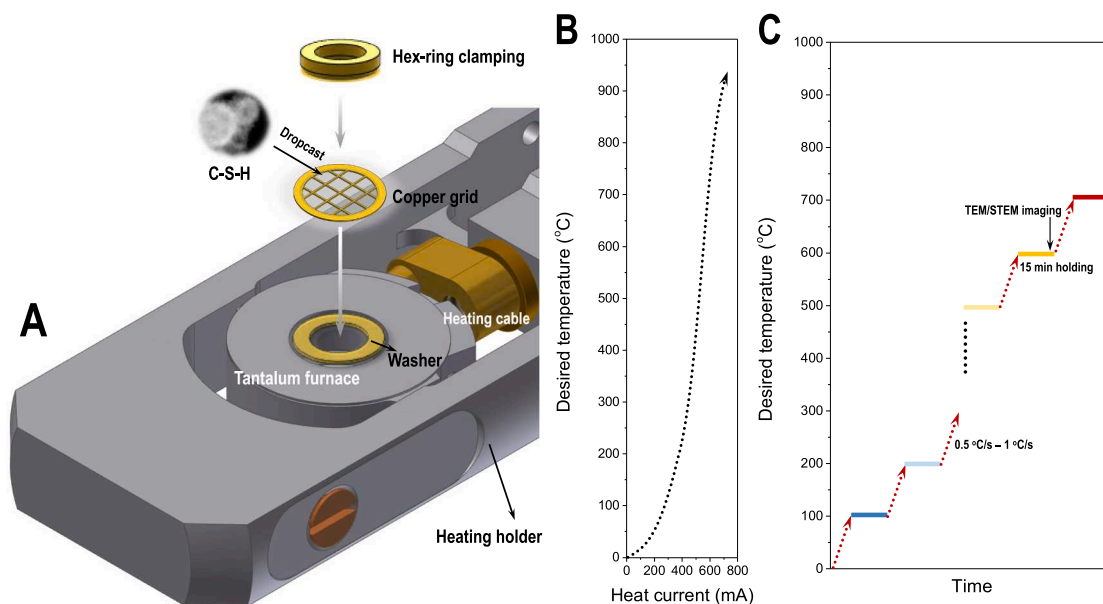**Fig. 1.** *In situ* heating under TEM and sample preparation. (A) Gatan 652 heating holder equipped with a tantalum furnace (https://www.gatan.com/products/tem-specimen-holders/heating-situ-holders). (B) The nonlinear relationship between the desired temperature and heat current. (C) Temperature history in the *in situ* heating experiment.

3. Results and discussions

3.1. Characterization of C-S-H gel

Hydrated C-S-H gel usually exhibits a foil-like morphology at a high solid to water ratio [17]. In Fig. 2A, these ultrathin C-S-H nanosheets tend to curl, wrinkle and accumulate together to form the silicate network. Multiscale pores can be observed and distinguished: (1). gel pores from C-S-H packing at nanometer size, and (2). large pores from the block voids at several hundred nanometers of size. Note that inter-layer pores at single nm size may be captured at a higher magnification (see Supporting Information). The gel exhibits a uniform distribution of calcium and silicon elements, with a calcium to silicate ratio of 1.38 found by fitting the EDS spectrum (Fig. 2B). X-ray diffraction (XRD) pattern shows that C-S-H (Fig. 2C) has a poor crystallinity with

characteristic broad peaks at 29.8°, 31.7°, and 51.9°. This is consistent with the previous report that C-S-H is known to be disordered at the atomic scale with defected silicate chains [18]. For tobermorite minerals [19] and synthetic crystalline C-S-H with a better a crystallinity [20], a typical basal peak located at 7.8° may be observed, which arises from the (200) reflection plane with a basal spacing of 11 Å. Since portlandite can precipitate in this work, these residual crystals are found to display extremely intense peaks in contrast to amorphous C-S-H gel. Characteristic vibration bands from the silicate chain in C-S-H are resolved in the FTIR spectrum (Fig. 2D). The band at $\sim$970 cm^{-1} is assigned to Si—O stretching vibrations of the Q^2 tetrahedra, while a small band at 810 cm^{-1} is attributed to Si—O stretching of Q^1 tetrahedra [21]. Notably, the Si-O-Si bending band at 670 cm^{-1} reflects the polymerization degree and structural order. A band at $\sim$450 cm^{-1} is due to the internal deformation of SiO$_4$ tetrahedra. The sample is well preserved without
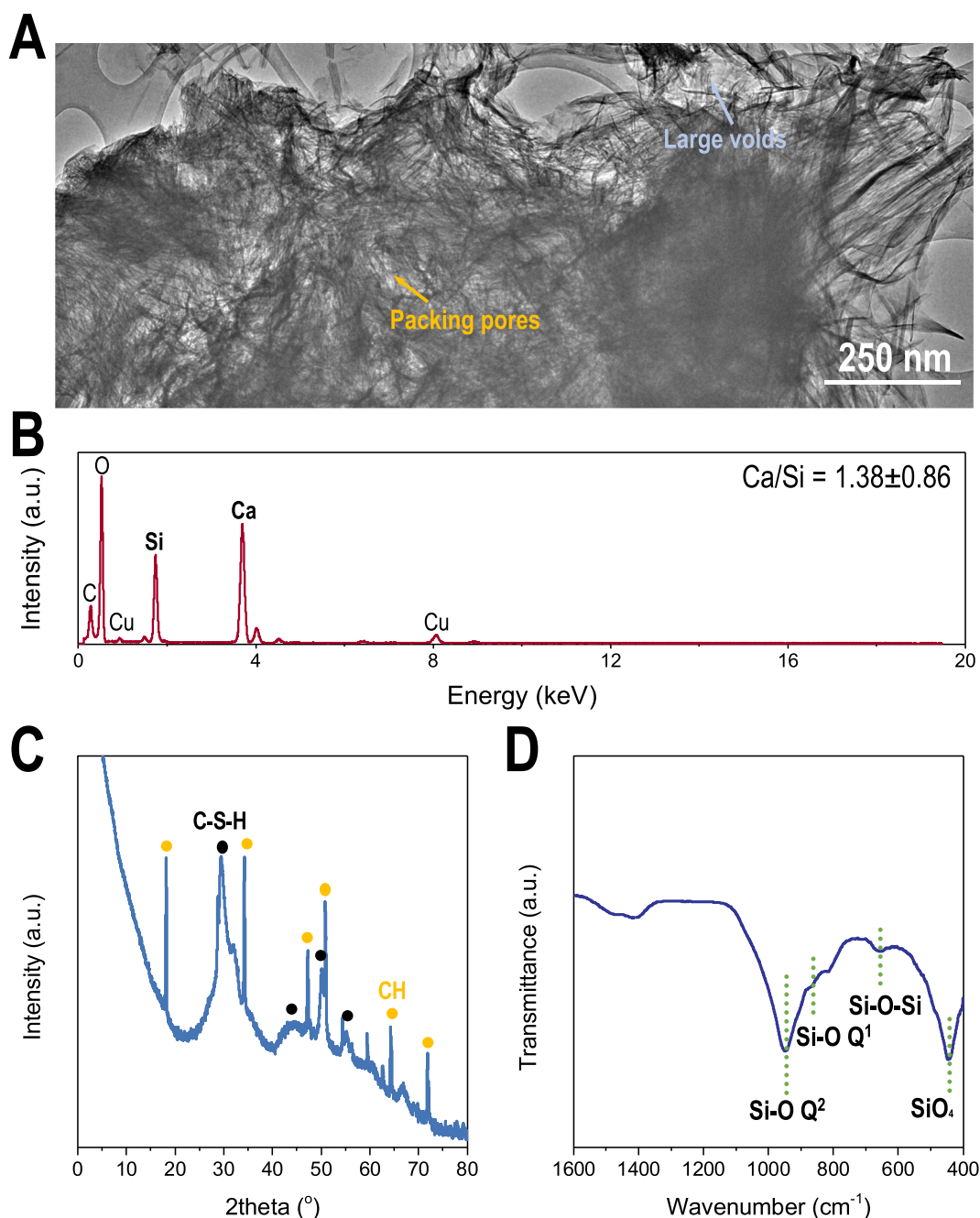

Fig. 2. Characterizations of C-S-H gel used in our experiment. (A) TEM image and (B) EDS spectrum, (C) XRD pattern, (D) FTIR spectrum of hydrated C-S-H.

carbonation as no pronounced calcite peaks and bands are distinguished [22], and all the preceding features are consistent with reported C-S-H structures.

Concerning the thermal properties of C-S-H, the dehydration reactions were examined in Fig. 3. The dehydration of C-S-H occurs throughout the entire heating period, exhibiting a sequential decrease in mass with increasing temperature. For example, the first weight loss between 100 and 200 °C corresponds to the removal of physically bound water in C-S-H pores [10]. The second significant weight loss at ~450 °C is attributed to portlandite dehydroxylation [11]. Specifically, decarbonation reactions from the decomposition of calcium carbonate are expected to occur at 800 °C [7].

3.2. Morphology evolution of C-S-H island with heating

We imaged C-S-H at ten different temperatures between 20 and 800 °C using scanning TEM (STEM), and these images are shown in Fig. 4. A C-S-H island at the microscale is formed when the C-S-H foils aggregate together. C-S-H still exhibits fundamentally layered; C-S-H nanosheets can be clearly distinguished at even 800 °C, indicating its good thermal stability. No obvious transition or shape change was observed from 20 to 200 °C during the physically bound water loss. Although the structural integrity is retained, the C-S-H island shrinks at higher temperatures. Some cracks are enlarged with a further opening when the sample temperature increases to 600 °C. Consequently, the C-S-H island becomes denser and more compact due to localized shrinkage and agglomeration.

The morphological evolution of the C-S-H island was investigated using quantitative analysis methods. The C-S-H boundary was detected by segmentation of the 8-bit STEM image through a gray value threshold algorithm [23]. The contour of the C-S-H island at various temperatures is shown in Fig. 5A. The entire island shrinks without falling into small fragments. The C-S-H area evolution can be divided into several stages, as shown in Fig. 5B. These stages are: (1). an activation stage below 200 °C, (2). a steady shrinkage period between 200 and 400 °C with small area fluctuations, and (3). a sharp shrinkage stage when the temperature is above 500 °C. These findings relate well to the reactions of C-S-H at different temperatures. For example, there is a slight thermal expansion in the induction period at 50 °C, with an area increasing by 1.5%, from 39.1 to 39.7 μm^2. The loss of physically bound water below 200 °C is a dynamic process without damage to the C-S-H structure, leading to a minor morphological change. However, chemical dehydration in C-S-H is crucial to the structure because of the strong driving force and irreversible transformation from high temperatures. The loss of gel water and interlayer water can result in the collapse of the C-S-H structure [24], consistent with the rapid area shrinkage in our work at temperatures over 500 °C.

The measurement of the perimeter as a function of temperature is shown in Fig. 5C. Overall, the perimeter decreases as the temperature is increased, dropping from 81.1 to 44.3 μm. An abnormal increase in the perimeter is found between 400 and 600 °C owing to more edges and fractures exposed at the boundary (Fig. 5A highlighted in arrows). We also evaluated some other shape descriptors like roundness and solidity. Note that the roundness was calculated by $4 * Area/(\pi * major\ axis^2)$ while solidity was defined by $\frac{Area}{Convex\ area}$. More details can be found in Supporting Information. 400 °C is a critical temperature and it is often regarded as the onset temperature for losing chemical water in the C-S-H structure [10]. Our in situ heating experiment suggests that the C-S-H particle may undergo surface reconstructions and rearrangements upon the loss of chemical water, which is presumably due to more exposed edges and terraces when the C-S-H blocks collapse and break down into parts. On the other hand, the increased roundness demonstrates that irregular C-S-H island opts to accumulate and shrink to spherical particles (Fig. 5D), regulated by surface energy minimization. Higher solidity indicates the structure is more compact with inner pores filled, which can represent the densification of inner C-S-H substance (Fig. 5E), and it can be explained by a higher packing density related to thermal shrinkage and conglobation aforementioned. Rather than indirect characterizations and possible assumptions on the C-S-H heating process, direct observation via TEM offers solid evidence on transformations and more quantitative information such as area and shape-related dynamics.

3.3. Pore structure evolution of C-S-H island

The pore structure is one of the key factors influencing the structural properties of concrete. High temperatures can induce micro and macro cracks in concrete structures, which deteriorate the performance. A rectangular pore in 810 × 630 nm was studied through real-time imaging at various temperatures (Fig. 6). Strikingly, no obvious expansion and spalling were observed while it displays autogenous shrinkage and self-healing behaviors. The rectangular pore is curing gradually in a homogeneous manner with C-S-H pieces moving from the substrate to the void space. It is found that the inner pore was almost refilled at 800 °C and the foil-like features of C-S-H remained intact.

Fig. 7A demonstrates a remarkable pore shrinkage under different temperatures. High temperature facilitates pore closure as the initial pore diameter over 600 nm gently decreases to ~500 nm when the temperature is below 700 °C and it rapidly shrinks to ~350 nm at 800 °C. Generally, heating at high temperatures can promote the repolymerization of silica chains [25], leading to a reorganization of coterminous C-S-H in adjacent regions. Subsequently, deformation, construction, and shrinkage in C-S-H blocks may narrow the pores in between. The average pore area shrinkage rate is estimated at $1.08 \times 10^3\ nm^2/°C$ and different shrinkage rates can be found at three stages, shown in Fig. 7B, C. For example, the steady period between 20 and 200 °C displays a $2 \times 10^3\ nm^2/°C$ rate followed by a "brake" stage with the shrinkage rate approaching $0.3 \times 10^3\ nm^2/°C$, ranging from 200 to 600 °C. As the temperature rises to 700 °C, the rate reaches its maximum up to $4 \times 10^3\ nm^2/°C$. In Fig. 7D, the roundness shows no direct correlation with the temperature. This is consistent with the observed irregularity in the contours of pores (Fig. 7A). In contrast, the pore solidity is more sensitive to temperatures. It keeps increasing at higher temperatures, which indicates the pore is gradually covered by C-S-H fabric. Thus, we found that solidity can characterize the densification period as
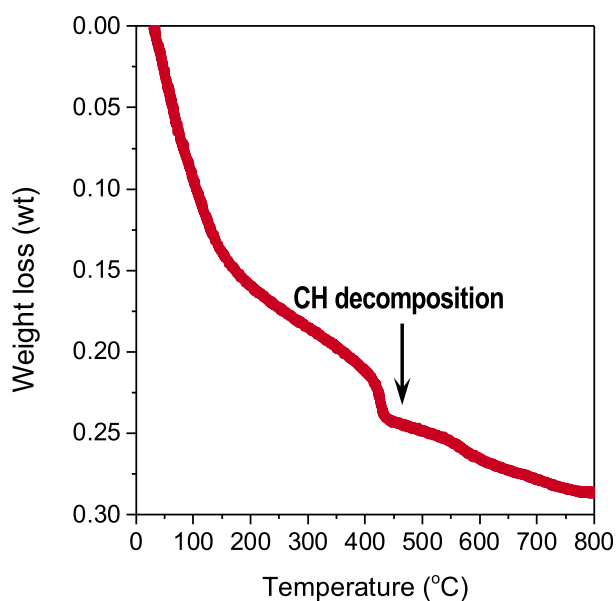

Fig. 3. A thermogravimetric analysis (TGA) curve of hydrated C-S-H (the water to solid ratio is 100:1) at various temperatures ranging from 20 to 800 °C.
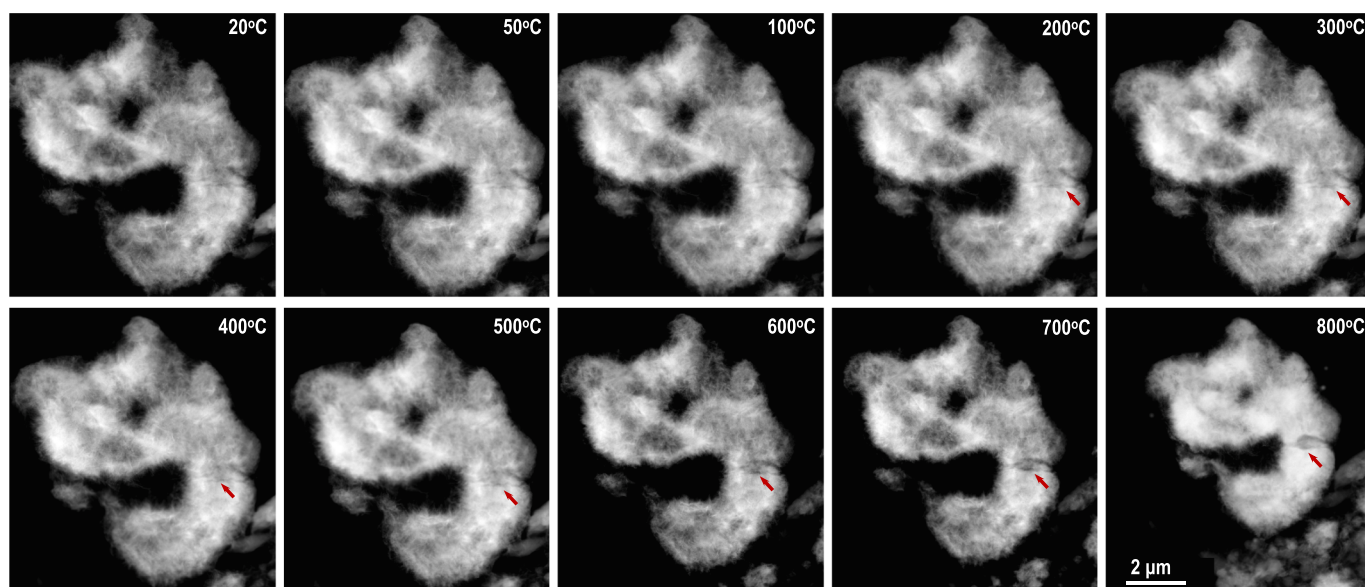
Fig. 4. Morphological evolution of C-S-H island at different temperatures ranging from 20 to 800 °C. Some cracks are highlighted in arrows.
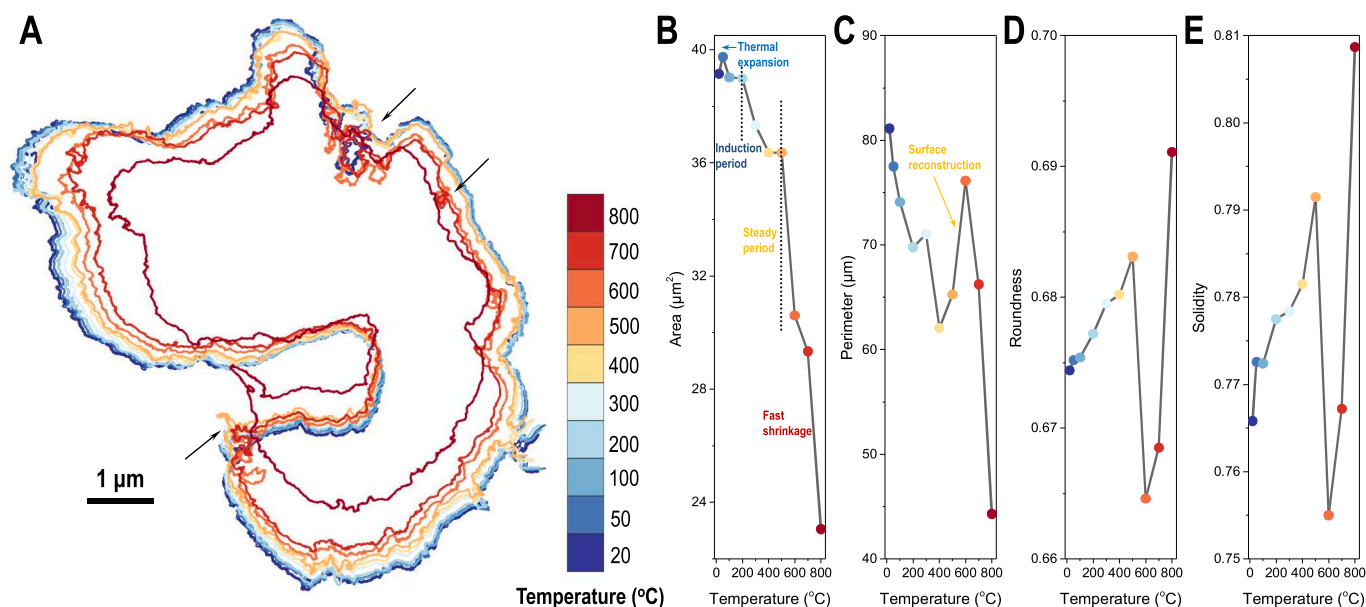

Fig. 5. Quantitative analysis of C-S-H island during the heating process. (A) Contours of C-S-H island color-coded by temperatures. Variations of shape descriptors such as (B) area, (C) perimeter, (D) roundness, and (E) solidity under different temperatures. Colors in (B-E) correspond to different temperatures as indicated in (A).

well as reflect the pore filling process, and it would be a promising descriptor to reveal the pore evolution during the *in situ* heating experiment.

3.4. Elemental variations at different temperatures

In Fig. 8A, C-S-H shows a uniform distribution of calcium and silicon elements with a Ca/Si ratio equaling to 1.38. However, the identical region in Fig. 8B exhibits more inhomogeneous features as the calcium atoms tend to accumulate locally. Moreover, the Ca/Si ratio decreases with increasing temperature in Fig. 8C. It is noted that the Ca/Si ratio is constant at ~1.3 below 100 °C while it dramatically drops at higher temperatures between 200 and 400 °C, which can be explained by the precipitation of the CaO phase. The spherical CaO nanoparticles are found in either STEM (Fig. 8B, HADDF) or TEM images (Fig. 8D). The sample is reexamined after annealing at 400 °C for 9 h. These CaO

nanoparticles are randomly distributed on the C-S-H substrate and the maximum size imaged was ~170 nm (Fig. 8E). Calcium diffusion is ordinary in leaching [26] and carbonation conditions [27] as the bonding of calcium ions in C-S-H, especially the interlayer atoms, is relatively weak. Considering the high vacuum state inside the TEM column coupled with high temperature, calcium may diffuse from the C-S-H structure and precipitates as CaO, leading to lower Ca/Si ratios. There's no apparent difference in the Ca/Si ratio at low temperatures, which is consistent with Gallucci's results [28]. However, our finding of a higher Ca/Si ratio at higher temperatures contradicts the work reported [29], which concluded that a higher Ca/Si ratio was obtained at high temperatures. The underlying reason may be that our experiment is based on highly purified C-S-H gel, while their investigation focused on the Portland cement system with supplement cementitious materials. The phase transition and diagram would be different in the presence of element impurities such as aluminum and iron ions and other mixtures
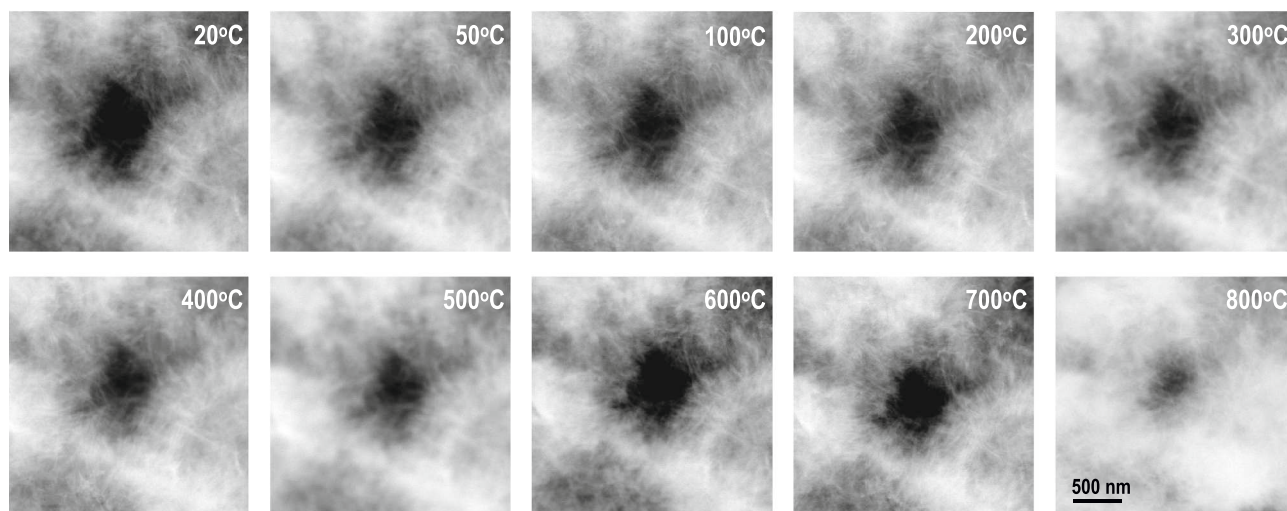
Fig. 6. Pore structure evolution in C-S-H island at different temperatures ranging from 20 to 800 °C. Note that the black region represents the pore which is ~500 nm in length.
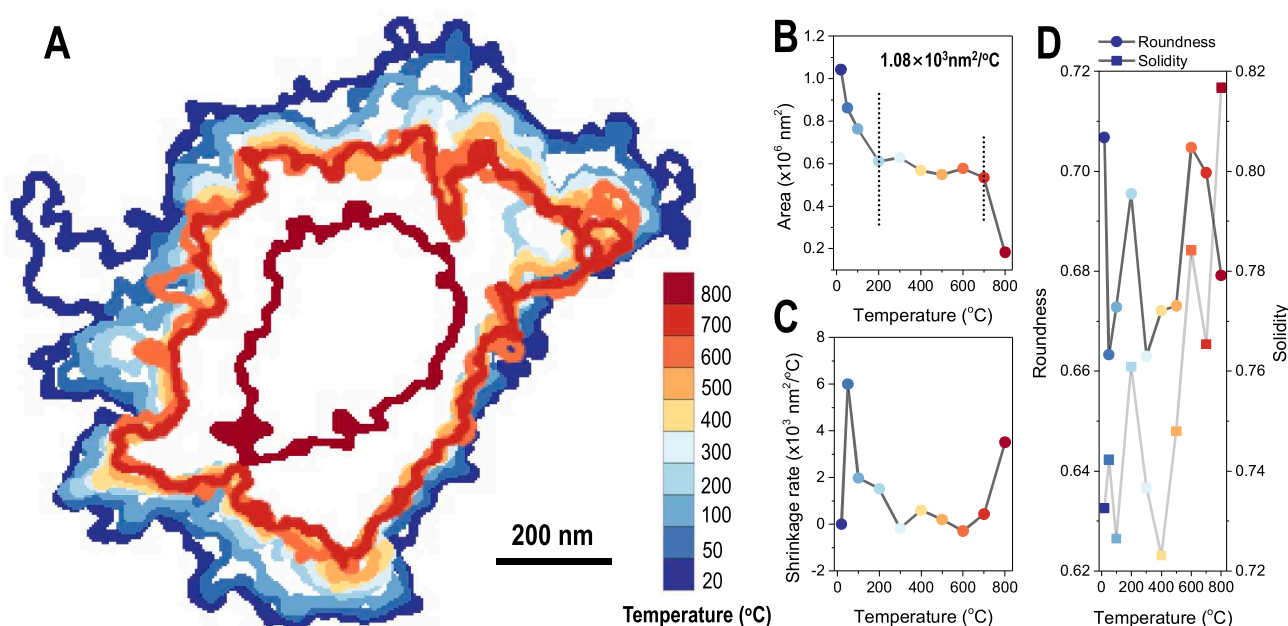

Fig. 7. Quantitative analysis of nanosized pore evolution during the heating process. (A) Contours of pore color-coded by temperatures. (B) Pore area variation and (C) its respective shrinkage rate under different temperatures. (D) Relation of roundness, solidity *versus* evaluated temperatures. Colors in (B—D) correspond to different temperatures as indicated in (A).

like portlandite and ettringites. In our monophase C-S-H *in situ* heating experiment, a downward trend of the Ca/Si ratio with increasing temperature was observed.

3.5. Phase transformation of C-S-H during heating

Monitoring the phase transformations during heating is essential to understand the mechanisms of C-S-H degradation related to morphological evolution, structural shrinkage, element variations, *etc.* Because some reactions occupy a small amount (less than 5%), conventional thermal analysis cannot resolve the kinetics with a low signal-to-noise ratio in the averaged measurement. Superior to TG/DSC and high-temperature XRD, our *in situ* selected area electron diffraction (SAED) focused on one small region with the more detailed information provided. In Fig. 9, the illuminated area is estimated at 5.6 μm² (~7.3 ×

10^{-3} ng in weight) and a series of electron diffraction patterns were recorded. Besides, the diffraction patterns are visualized as a function of azimuthal angle (φ) and *d* spacing (*k*) in polar coordinate, with radial intensity profiles derived, and plotted in Fig. 9B, E and Fig. 9C, F, respectively.

The crystal structure of C-S-H resembles tobermorite [30], and some signature fringes of C-S-H are distinguishable at room temperature, such as (022) at 3.3 nm^{-1} and (026) at 4.2 nm^{-1}. We found that these fringes intensify at higher temperatures. Some foreign spots with strong intensity are observed as well above 400 °C, implying the phase transformation of C-S-H. At 600 °C, the spots are scattered instead of displaying a "halo" diffusion ring at 20 and 50 °C, indicating the formation of nanoscale polycrystals.

According to Fig. 10A, reactions can be inferred based on the occurrence of characteristic peaks. For example, there is no phase
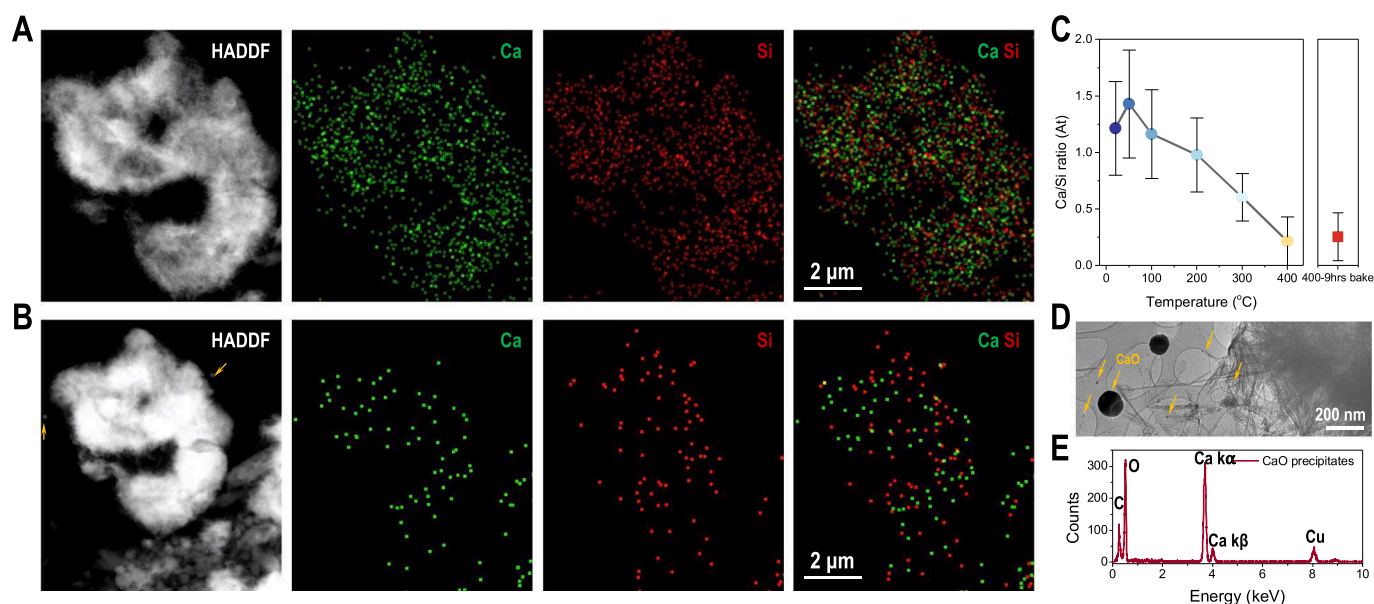
Fig. 8. Elemental analysis of C-S-H gel under different temperatures. HADDF image and EDS mapping of C-S-H island at (A) 20 °C and (B) 400 °C after 9 h' baking at 400 °C. The imaging mode, element types, and element overlaps are labeled at the right corners. (C) The evolution of Ca/Si ratio (atom mole) under different temperatures. The error bar is from the multiple measurements at different regions. (D) CaO precipitates after high-temperature firing (9 h' baking at 400 °C). (E) EDS spectrum of CaO precipitates.

transition between 20 and 50 °C where no new peaks appeared. However, at a medium temperature of 300 °C, the structure of C-S-H changes quickly as the peak position shifts and intensity rises. This can be interpreted that the silicate skeleton reorganizes when the structural water is removed upon heating. High temperature can even facilitate the re-polymerization in silicate chains, resulted in Q^3, Q^4 species [25]. The reaction becomes more complicated when the temperature reaches 400 °C with many new peaks showing up. These peaks can be assigned to calcium silicon-based minerals [31], which indicates the partial decomposition of C-S-H and recrystallization of calcium silicate oxides at high temperatures. Heating supplies extra energy to overcome the energy barrier for possible phase transformations from the thermodynamics perspective. Here, full width at half maximum (FWHM) at ~3 nm^{-1}, a signature peak for (022), was introduced to characterize the crystallinity degree. A decreasing FWHM can indicate an increase in the degree of crystallinity or an increase in the grain size. Fig. 10B shows that the FWHM declines at higher temperatures, demonstrating an amorphous-to-crystalline transformation in C-S-H, either in the poly-crystal or nanocrystal forms. In Fig. 10C, the "phase transformation" was determined when an extra peak appears during the heating at evaluated temperatures. The consensus is that heating provides an additional driving force and promotes chemical reactions. This coincides with our results that C-S-H is prone to transform at higher temperatures. C-S-H can even transform into wollastonite at a temperature of over 850 °C [13,32]. Some techniques such as high temperature XRD or neutron diffraction can be the powerful alternatives to resolve the crystallization and transformation of C-S-H during the heating process [12,13,33].

4. Conclusions

The evolution of C-S-H at various temperatures was investigated by *in situ* heating in the TEM. The nanoscale morphology, pore structure, element distribution, and phase transformation were correlated with evaluated temperatures. Some conclusions can be reached as follows:

(1) The shrinkage of the C-S-H island was directly visualized at an average rate of 0.02 μm^2/°C. The whole process can be divided into three stages: induction period, steady period, and rapid shrinkage period accompanied by conglobation and densification of C-S-H foils.
(2) Nanoscale pores can be healed at high temperatures. An 810 × 630 nm^2 rectangular pore can be filled at a speed of 1.08×10^3 nm^2/°C. Heating facilitates the re-polymerization and reconstruction in C-S-H blocks.
(3) Ca/Si ratio declines at higher temperatures. Calcium ions tend to be released from the C-S-H structure upon heating by precipitating CaO nanocrystals.
(4) Phase transformation was detected by real-time electron diffraction. The decomposition of C-S-H and recrystallization of calcium silicate minerals are distinguished. The crystallinity evolution was examined as well.

Nanoscale mechanisms of the degradation of C-S-H after firing were revealed through *in situ* experiments from chemistry and thermodynamics perspectives. Our work opens up opportunities to design high-performance concrete serving at high-temperatures.

CRediT authorship contribution statement

Q.Z. designed and performed the experiments and analyzed the experimental data. X.L. carried out the XRD, FTIR, and TG measurements. K.B. helped with TEM alignments and TEM imaging. Q.Z. wrote the manuscript. All authors contributed to the overall scientific interpretation and editing of the manuscript. All work was carried out under the supervision of J.J and H.Z.

Data availability

Data are available in the online version of this paper. Data that support the findings of this study are available from corresponding authors upon reasonable request.

Code availability

Computer codes for calculations in this work are available upon request from the corresponding authors.
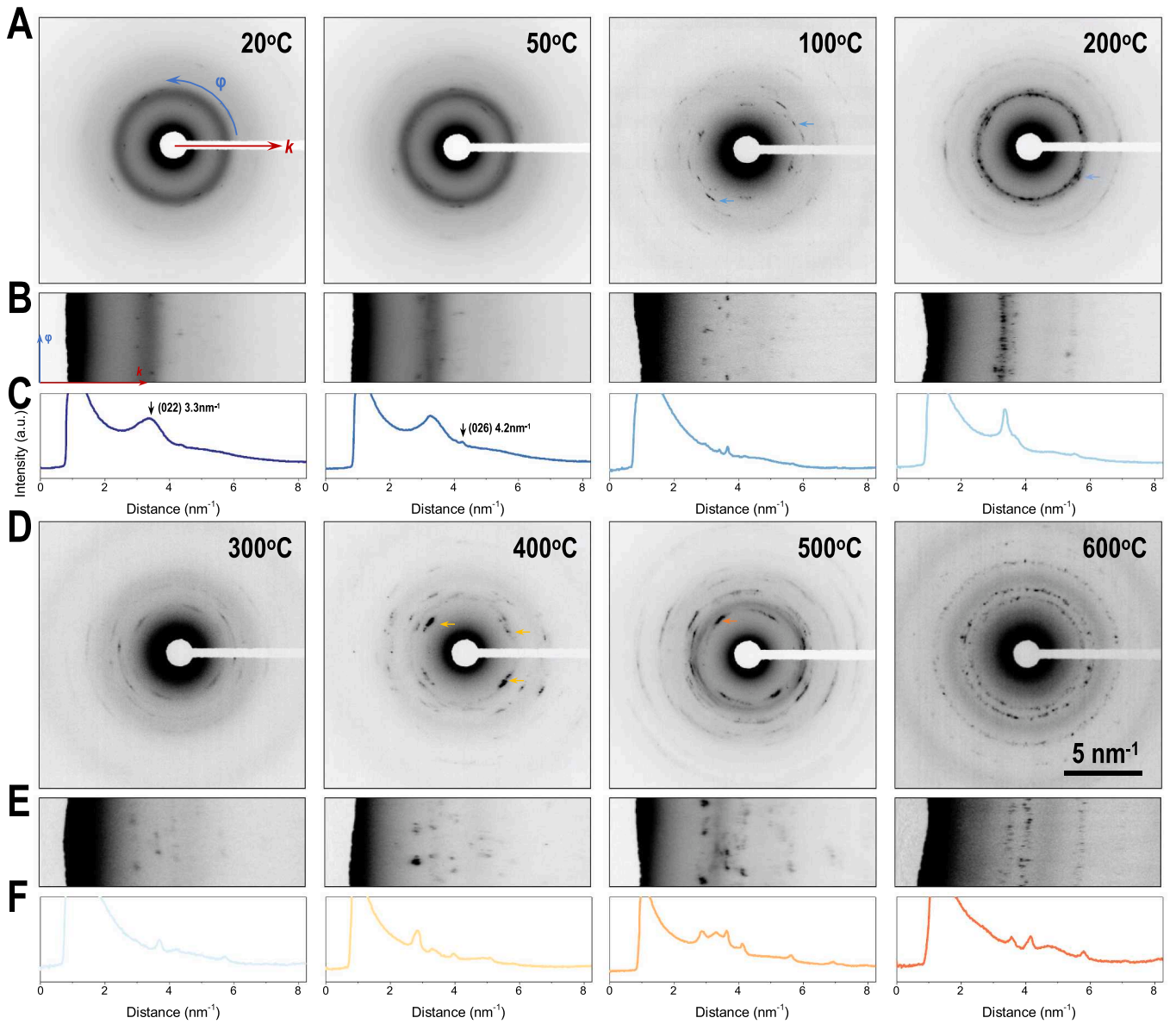
Fig. 9. Phase transition and crystallinity evolution of C-S-H during the heating process. (A, D) Electron diffraction patterns, (B, E) azimuthal projection, and (C, F) radial intensity profiles of C-S-H at evaluated temperatures.
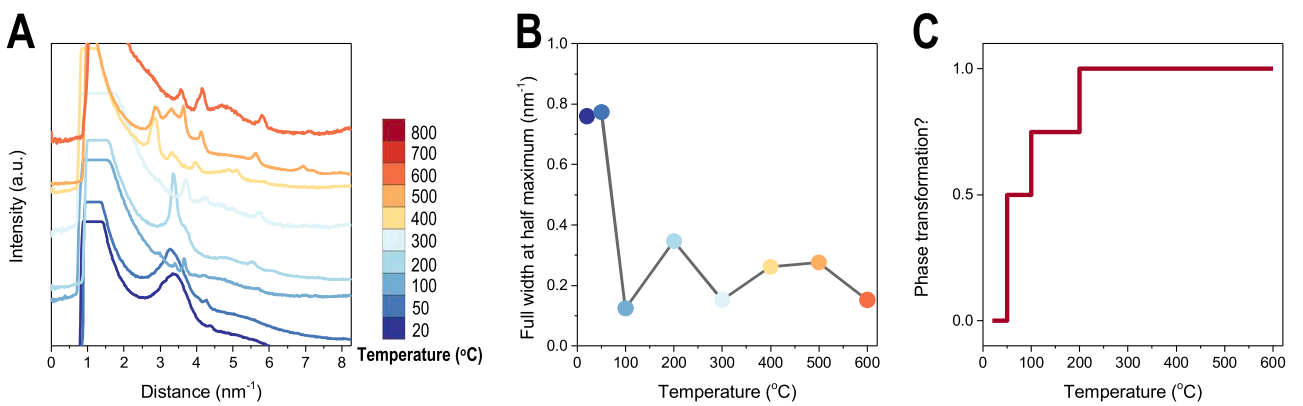

Fig. 10. Qualitative analysis of C-S-H transition and crystallinity evolution during the heating process. (A) Radial intensity profile, (B) FWHM, and (C) possibility of phase transformation of C-S-H at different temperatures.

Declaration of competing interest

The authors declare no competing interests.

Acknowledgments

Appendix A. Supplementary data

Supplementary data to this article can be found online at https://doi.org/10.1016/j.cemconres.2021.106579.

References

[1] A. Lau, M. Anson, Effect of high temperatures on high performance steel fibre reinforced concrete, Cem. Concr. Res. 36 (2006) 1698–1707.

[2] H. Tanyildizi, A. Coskun, The effect of high temperature on compressive strength and splitting tensile strength of structural lightweight concrete containing fly ash, Constr. Build. Mater. 22 (2008) 2269–2275.

[3] K. Sakr, E. El-Hakim, Effect of high temperature or fire on heavy weight concrete properties, Cem. Concr. Res. 35 (2005) 590–596.

[4] I. Hager, Behaviour of cement concrete at high temperature, Bull, Polish Acad. Sci. Tech. Sci. 61 (2013) 145–154.

[5] I.G. Richardson, The calcium silicate hydrates, Cem, Concr. Res. 38 (2008) 137–158.

[6] Q. Zheng, J. Jiang, J. Yu, X. Li, S. Li, Aluminum-induced interfacial strengthening in calcium silicate hydrates: structure, bonding, and mechanical properties, ACS Sustain, Chem. Eng. 8 (2020) 2622–2631, https://doi.org/10.1021/acssuschemeng.9b04862.

[7] L. Alarcon-Ruiz, G. Platret, E. Massieu, A. Ehrlacher, The use of thermal analysis in assessing the effect of temperature on a cement paste, Cem. Concr. Res. 35 (2005) 609–613.

[8] L.P. Esteves, On the hydration of water-entrained cement–silica systems: combined SEM, XRD and thermal analysis in cement pastes, Thermochim. Acta 518 (2011) 27–35.

[9] I. Pane, W. Hansen, Investigation of blended cement hydration by isothermal calorimetry and thermal analysis, Cem. Concr. Res. 35 (2005) 1155–1164.

[10] C. Alonso, L. Fernandez, Dehydration and rehydration processes of cement paste exposed to high temperature environments, J. Mater. Sci. 39 (2004) 3015–3024.

[11] Q. Zheng, J. Jiang, G. Xu, J. Yu, L. Tang, S. Li, New insights into the role of Portlandite in the cement system: elastic anisotropy, thermal stability, and structural compatibility with CSH, Cryst, Growth Des. 20 (2020) 2477–2488.

[12] M. Castellote, C. Alonso, C. Andrade, X. Turrillas, J. Campo, Composition and microstructural changes of cement pastes upon heating, as studied by neutron diffraction, Cem. Concr. Res. 34 (2004) 1633–1644.

[13] E.T. Rodriguez, K. Garbev, D. Merz, L. Black, I.G. Richardson, Thermal stability of CSH phases and applicability of Richardson and Groves' and Richardson C-(A)-SH (I) models to synthetic CSH, Cem. Concr. Res. 93 (2017) 45–56.

[14] S. Breuer, M. Schwotzer, S. Speziale, F.R. Schilling, Thermoelastic properties of synthetic single crystal portlandite Ca (OH) 2-Temperature-dependent thermal diffusivity with derived thermal conductivity and elastic constants at ambient conditions, Cem. Concr. Res. 137 (2020), 106199.

[15] D. Dauti, A. Tengattini, S. Dal Pont, N. Toropovs, M. Briffaut, B. Weber, Analysis of moisture migration in concrete at high temperature through in-situ neutron tomography, Cem. Concr. Res. 111 (2018) 41–55.

[16] X. Li, A. Ouzia, K. Scrivener, Laboratory synthesis of C 3 S on the kilogram scale, Cem. Concr. Res. 108 (2018) 201–207.

[17] Q. Zheng, J. Jiang, C. Chen, J. Yu, X. Li, L. Tang, S. Li, Nanoengineering microstructure of hybrid C–S–H/silicene gel, ACS Appl. Mater. Interfaces 12 (2020) 17806–17814.

[18] M.J.A. Qomi, K.J. Krakowiak, M. Bauchy, K.L. Stewart, R. Shahsavari, D. Jagannathan, D.B. Brommer, A. Baronnet, M.J. Buehler, S. Yip, Combinatorial molecular optimization of cement hydrates, Nat. Commun. 5 (2014) 4960.

[19] S.A. Hamid, The crystal structure of the 11 Å natural tobermorite Ca2. 25 [Si3O7. 5 (OH) 1.5]· 1H2O, Zeitschrift Für Krist. Mater. 154 (1981) 189–198.

[20] S. Grangeon, F. Claret, C. Roosz, T. Sato, S. Gaboreau, Y. Linard, Structure of nanocrystalline calcium silicate hydrates: insights from X-ray diffraction, synchrotron X-ray absorption and nuclear magnetic resonance, J. Appl. Crystallogr. 49 (2016) 771–783.

[21] P. Yu, R.J. Kirkpatrick, B. Poe, P.F. McMillan, X. Cong, Structure of calcium silicate hydrate (C-S-H): near-, mid-, and far-infrared spectroscopy, J. Am. Ceram. Soc. 82 (1999) 742–748.

[22] S. Gunasekaran, G. Anbalagan, S. Pandi, Raman and infrared spectra of carbonates of calcite structure, J. Raman Spectrosc. An Int. J. Orig. Work All Asp. Raman Spectrosc. Incl. High. Order Process. Also Brillouin Rayleigh Scatt. 37 (2006) 892–899.

[23] J.-C. Yen, F.-J. Chang, S. Chang, A new criterion for automatic multilevel thresholding, IEEE Trans. Image Process. 4 (1995) 370–378.

[24] J.I. Escalante-Garcıa, J.H. Sharp, The microstructure and mechanical properties of blended cements hydrated at various temperatures, Cem. Concr. Res. 31 (2001) 695–702.

[25] D. Hou, D. Li, T. Zhao, Z. Li, Confined water dissociation in disordered silicate nanometer-channels at elevated temperatures: mechanism, dynamics and impact on substrates, Langmuir. 32 (2016) 4153–4168.

[26] M. Mainguy, C. Tognazzi, J.-M. Torrenti, F. Adenot, Modelling of leaching in pure cement paste and mortar, Cem. Concr. Res. 30 (2000) 83–90.

[27] J. Jiang, Q. Zheng, D. Hou, Y. Yan, H. Chen, W. She, S. Wu, D. Guo, W. Sun, Calcite crystallization in the cement system: morphological diversity, growth mechanism and shape evolution, Phys. Chem. Chem. Phys. 20 (2018) 14174–14181.

[28] E. Gallucci, X. Zhang, K.L. Scrivener, Effect of temperature on the microstructure of calcium silicate hydrate (CSH), Cem. Concr. Res. 53 (2013) 185–195.

[29] Z. Jia, C. Chen, J. Shi, Y. Zhang, Z. Sun, P. Zhang, The microstructural change of CSH at elevated temperature in Portland cement/GGBFS blended system, Cem. Concr. Res. 123 (2019), 105773.

[30] P. Paradiso, R.L. Santos, R.B. Horta, J.N.C. Lopes, P.J. Ferreira, R. Colaço, Formation of nanocrystalline tobermorite in calcium silicate binders with low C/S ratio, Acta Mater. 152 (2018) 7–15.

[31] C.C. Dharmawardhana, A. Misra, W.-Y. Ching, Quantum mechanical metric for internal cohesion in cement crystals, Sci, Rep. 4 (2014) 1–8.

[32] K. Garbev, M. Bornefeld, G. Beuchle, P. Stemmermann, Cell dimensions and composition of nanocrystalline calcium silicate hydrate solid solutions. Part 2: X-ray and thermogravimetry study, J. Am. Ceram. Soc. 91 (2008) 3015–3023.

[33] S. Im, H. Jee, H. Suh, M. Kanematsu, S. Morooka, K. Taku, N. Yuhei, A. Machida, J. Kim, S. Bae, Temperature effects on local structure, phase transformation, and mechanical properties of calcium silicate hydrates, J. Am. Ceram. Soc. (2021).